Experimental analysis of the floor inclination effect on the turbulent wake developing behind a wall mounted cube

Maria Ikhennicheu, Benoit Gaurier, Philippe Druault, Gregory Germain

Experimental analysis of the floor inclination effect on the turbulent wake developing behind a wall mounted cube

Maria Ikhennicheu [1a], Benoît Gaurier[a], Philippe Druault[b], Grégory Germain[a]

[a]*Ifremer, Marine Structure Laboratory, 150 Quai Gambetta 62200 Boulogne sur Mer, France. gregory.germain@ifremer.fr*
[b]*Sorbonne Universités, UPMC Univ Paris 06, CNRS, UMR 7190, Institut Jean Le Rond d'Alembert, F-75005 Paris, France. philippe.druault@upmc.fr*

Abstract

The present study aims at investigating turbulence characteristics in high flow velocity areas like those suitable for marine energy application. The Reynolds number, based on the rugosity height and mean flow velocity, is rather high: $R_e = 2.5 \times 10^7$. For that purpose, experiments are carried out in a flume tank with R_e as high as achievable in Froude similitude (in the tank: $Re = 2.5 \times 10^5$ and $Fr = 0.23$). Obstacles are canonical wall-mounted elements chosen to be representative of averaged bathymetric variations: a cube and a cube followed by an inclined floor. First, the wake topology past a canonical wall-mounted cube is illustrated from PIV measurements. Results show a flow behaviour already observed in the literature but for different upstream conditions (R_e and turbulence intensity). Second, the impact of the addition of an inclined floor is studied. It is shown that the inclination causes a squeezing of the cube wake that strongly impacts the shape and intensity of the shear layer (up to 10% more intense with the inclined floor). To fully grasp the turbulence organization in the wake for both test cases, an analysis using both complementary Proper Orthogonal Decomposition and quadrant method is performed. POD acts as a turbulent noise filter and quadrant method decomposes turbulent events. Results show the predominance of ejection (Q2) and sweep (Q4) events in the flow Reynolds shear stress. Q2 events are more energetic although Q4 events prevail. It is observed that the inclined floor causes a persistence of Q2 and Q4 events higher into the water column, more than the impulsion given by the floor altitude variations. The rise of the cube wake due to the inclined

---

[1]Corresponding author. E-mail: maria.ikhennicheu@ifremer.fr

floor is thus illustrated using Q4 predominance area.

1. Introduction

The idea of harvesting energy from the sea dates back to antiquity, however it is only recently that industrial projects have started to emerge. There is a strong tidal potential in France: over 20% of the European potential is located in French water, especially in the Alderney Race (*Raz-Blanchard*) that presents currents up to $U_{insitu} = 5m/s$. Surveys performed in this area give access to the bathymetry (see fig. 1) showing an average depth variation of $H_{insitu} = 5m$. The Reynolds number *in situ*, based on H_{insitu} and U_{insitu} and the kinematic viscosity of water ν, is high: $R_{e,insitu} = H_{insitu}U_{insitu}/\nu = 2.5 \times 10^7$. Such variations are causing a high turbulence rate in the water column, where marine current turbines are meant to be installed. Turbulence can have a major impact on the tidal turbines, on their production [9] and on the structural fatigue [18]. Before trying to reproduce complex structures, we chose to introduce the topic by studying elementary obstacles representatives of real life condition: *i.e.* with an aspect ratio of the magnitude of the mean bathymetry variations encountered between France and Alderney.
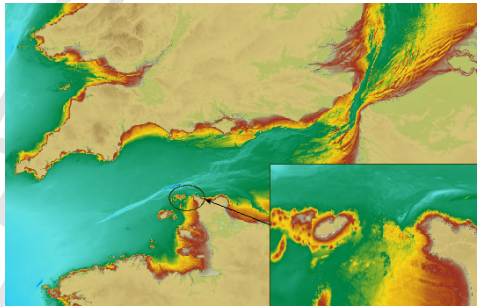

Figure 1: Bathymetry of the English Channel with a zoom of the Alderney Race area, SHOM [21]

The wall-mounted cube is a common obstacle studied in wind tunnels or water tanks. For this obstacle, we count the studies performed by Hearst et al. [10] at $R_e = 1.8 \times 10^6$ or Castro & Robins [6] going up to $Re = 10^5$,

2

both in wind tunnels. Hearst at al. [10] studied the impact of turbulence intensity on a wall-mounted cube and found that, when turbulence intensity increases the wake shortens with a stronger dissipation rate although the flow topology remains identical. McArthur et al. [15] studied the flow past Ahmed bodies at R_e up to 7.7×10^5 in air. However, few studies were achieved at high Reynolds number ($R_e > 10^5$). Hussein & Martinuzzi [11] and Martinuzzi & Troppea [14] are among the firsts to characterize the flow around a wall-mounted cube and describe its wake. In keeping with their work, Castro & Robins [6] highlighted the importance of the boundary layer thickness δ. It is fundamental to know where the obstacle intersects the boundary layer to characterize the incoming stress field. The angle of attack is studied by VanOudheusen et al. [23] using similar methods as the present study.

The cube is studied here as a mean bathymetric variation. In addition, smooth depth variation are observed at the sea bottom (see figure 1). No study on the impact of floor inclination after an obstacle was found in the literature. The closest studies to the present case are those carried out on dunes, such studies are summed up by Best [3]. However, most cases are for river dunes, hence for lower Reynolds number ($R_e < 10^3$, [3]) even if Sarkar & Mazmunder [20] carried out trials on dunes at $R_e = 1.4 \times 10^5$ in a small flume tank . Many studies on dunes underline the importance of turbulent events that can rise high in the water column [2, 20, 3]. The rise of turbulent structures can have a major impact on turbines used to extract tidal energy [9]. So, the knowledge of these high energetic flow structures is of great importance. In this study, experiments are carried out in a large flume tank to investigate the impact of an inclined floor on the wake of a wall-mounted cube. The question of the rise of turbulent events is investigated.

For this investigation and following previous works [5, 19], the Proper Orthogonal Decomposition [13] coupled with the quadrant analysis [25] is considered. POD application allows first the extraction of energetic flow structures of the turbulent flow. Second, these energetic structures are classified according to the Reynolds-stress values. That permits to detect events called ejection or sweep [25, 1]. In the present study, this coupled method is used to detect the influence of the addition of the inclined floor downstream of a wall-mounted cube on the turbulent flow characteristics. Note that to study the turbulent structures developing over dunes, Bennet & Best [2] used the quadrant analysis demonstrating that inclined floor located behind a dune promotes the formation of these events.

After a description of the experimental set-up and a brief explanation

3

of the POD method, experimental results are presented. First, a spatial description is made for the wall-mounted cube in a low turbulence intensity flow. Then, the impact of the addition of an inclined floor is studied through PIV measurements planes analysis and then using a coupled POD-quadrant method.

2. Experimental set-up

The tests are carried out in the wave and current circulating flume tank of IFREMER in Boulogne-sur-Mer presented in figure 2. The test section has the following dimensions: $18m$ length $\times$ $4m$ width $\times$ $2m$ height. The incoming flow is assumed to be steady and uniform. By means of grid and honeycomb (that acts as a flow straightener) placed at the inlet of the working section (see fig. 3(a)), a turbulent intensity of $I = 1.5\%$ can be achieved. In this study, non dimensional lengths are used: $x^* = x/H$, $y^* = y/H$ and $z^* = z/H$, with H the cube height.

In this work, we focus on the three instantaneous velocity components denoted (U, V, W) along the (X, Y, Z) directions respectively (Fig. 3(a)). The Reynolds decomposition is used allowing the decomposition of each instantaneous velocity component into a mean value and a fluctuation part: $U = \overline{U} + u'$, where an overbar indicates the time average. Turbulence intensity I in the incoming flow is defined as follows:

$$I = 100\sqrt{\frac{\frac{1}{3}(\overline{u'^2} + \overline{v'^2} + \overline{w'^2})}{\overline{U_\infty}^2 + \overline{V_\infty}^2 + \overline{W_\infty}^2}} \tag{1}$$

where $(\overline{U_\infty}, \overline{V_\infty}, \overline{W_\infty})$ are the uniform velocity components of the incoming flow. In the following, the denoted Reynolds shear stress component corresponds to $\tau_{uw} = \overline{u'w'}$ and the 2D turbulence kinetic energy is $k_{uw} = \frac{1}{2}(\overline{u'^2} + \overline{w'^2})$.

	Scale	U_∞ [m/s]	Rugosity height H [m]	Depth D [m]	$R_e = \frac{HU_\infty}{\nu}$	$F_r = \frac{U_\infty}{\sqrt{gD}}$
Alderney Race	1	5	5	40	2.5×10^7	0,25
Flume tank	1/20	1	0,25	2	2.5×10^5	0,23

Table 1: *in situ* and experimental conditions (1:20 scale)

4

All obstacles considered in this study are chosen to represent the real-life conditions at scale. In the tank, $I = 1.5\%$ is the lowest turbulence intensity achievable. Reynolds similitude could not be achieved so the experiments are carried out in a Froude similitude with a Reynolds number as high as achievable to be closer to real conditions, although Castro & Robins [6] found that for $R_e > 10^4$, the flow topology achieves a certain Reynolds number independence. Each element represents a key bathymetric element in the area of interest at a 1:20 scale (see table 1). The first set of experiments is carried out on a wall-mounted cube with height: $H = 250\ mm$. The following experimental set-up consists in the same wall-mounted cube with an additional inclined floor downstream of the cube. The floor is a $2m$ long $\times$ $1.2m$ wide plane with an inclination of $6.5°$ representing a smooth variation of the bathymetry that exists at site: it represents an average elevation of 12 meters of the floor over 105 meters. This choice also is a geometry easy to represent both experimentally and numerically for further comparisons [17, 4]. Furthermore, the floor inclination do not have much impact on the outer flow nor the surface elevation, only the near wake of the obstacle is impacted. The floor is disposed directly downstream of the cube. In the rest of this study, the flow configuration with the cube alone will be referred to as C_1 test case and the other flow configuration with both cube and inclined floor (6.5^o of inclination) will be referred to as C_1S_6 test case.
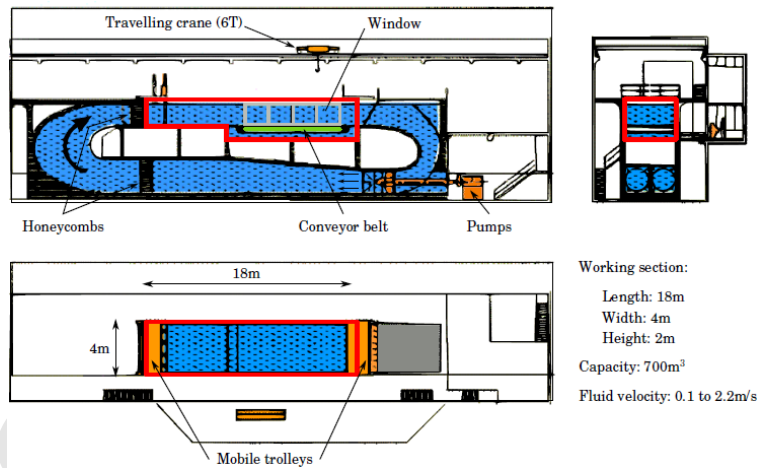

Figure 2: Ifremer Flume tank in Boulogne-sur-Mer

To characterize the flow, a Laser Velocimetry technique is used (see fig. 3(b)), the tank is seeded with 10 μm diameter micro-particles. For the

(a) Representation of the cube in the tank with (X,Y,Z) axis

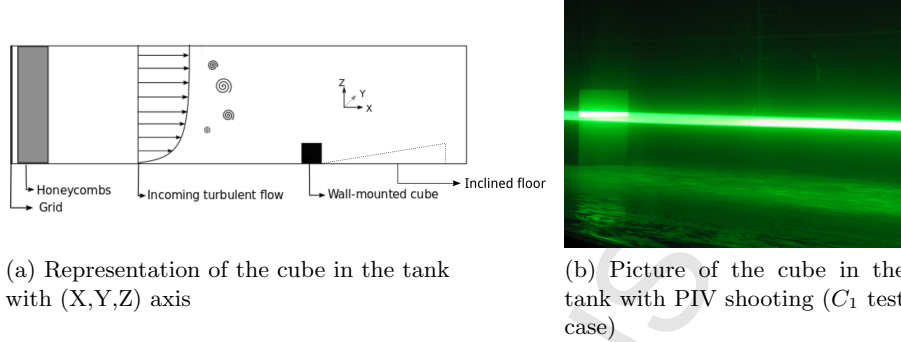(b) Picture of the cube in the tank with PIV shooting (C_1 test case)

Figure 3: Schematic view and picture of the cube in the wave and current circulating tank of IFREMER

PIV (Particle Image Velocimetry) measurements, a Nd-YAG Laser GEMINI-LIKE is used with a Camera FLOWSENS EO-2M 1600pix $\times$ 1200pix that makes double images with a time step of 800 μs. A particle is detected on 3 to 5 pixels. PIV acquisitions are made for $150s$, hence 2250 double images are taken with a $15H_z$ acquisition frequency. The data are post processed with the software DYNAMIC STUDIO. To get rid of noise, the mean image is first subtracted to all images. Then, the displacement of particles is calculated using a Cross-Correlation on a 32pix $\times$ 32pix interrogation windows with 50% overlap [16]. Outliers are replaced with the Universal Outlier Detection [26], depending on the plane, from 1% to 13% of the vectors are substituted. Single-pass method is used as, in our case, multipass adaptive PIV leads to errors generating artefacts rather than improving resolution. Two configurations are used for the PIV measurements:

- for horizontal planes, the laser lightens the ($z^* = 0.7$) plane of the fluid and the camera is placed above the obstacle, perpendicularly to the laser plane and the precision in term of pixel size is $0.21mm$ for case C_1 and $0.25mm$ for case C_1S_6,

- for vertical planes, the laser lightens the ($y^* = 0$) plane of the fluid and the camera is positioned beside the obstacle and the precision in term of pixel size is $0.43mm$.

Figure 4 illustrates the result of vertical PIV measurement after postprocessing with Dynamic Studio (Cross Correlation and Universal Outlier Detection) applied on the case C_1S_6, a mask is applied on the obstacles.
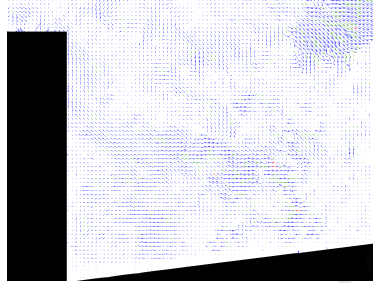
6

Figure 4: Instantaneous velocity field in a vertical PIV measurement plane, after post-precessing with DynamicStudio for case C_1S_6, a mask is applied on the obstacles

Figure 5 (a) and (b) show the 10 and 6 PIV vertical measurement planes related to C_1 and C_1S_6 test cases respectively and figure 5(c) shows the 6 PIV horizontal measurement planes carried out for C_1 only. In the following, when regarding the mean flow quantities, an interpolation is done between each consecutive plane allowing a representation of the mean quantities in the whole available domain.

3. Characterization of the wake behind wall-mounted obstacles

3.1. Reference case of the wall-mounted cube

This section focuses on the characterization of the reference case through a spatial and temporal analysis. Reference is chosen for the more canonical of all elements: the wall-mounted cube in a flow (case C_1) with high Reynolds number ($R_e = 2.5 \times 10^5$) and a Froude number of 0.23.

Using PIV measurements, streamlines are plotted in figure 6(a) for the vertical view and in figure 6(b) for the horizontal view. Figure 7 represents $\overline{U}$ maps in both cases. In these figures, the classical behaviour of the flow past a wall-mounted object can be seen [10, 27]: the flow separates at the leading edges of the cube into the outer steady region and the recirculation area downstream of the cube. A shear layer develops in-between and then the flow reattaches. The recirculation lengths are evaluated upstream (l_{us}), on top (l_{top}) and downstream (l_{ds}) of the cube. Results give, for the recirculation lengths, $l_{us}^* = 0.7$, $l_{top}^* = 0.4$ and $l_{ds}^* = 1.9$ and for the stagnation point altitude on the upstream face of the cube: $z_{st}* = 0.7$. These results are consistent with the conclusions given in [10] for $R_e = 10^6$ and also for lower Reynolds number $R_e \sim 10^4$ [11]. The horizontal view (fig. 6(b)) shows the two counter-rotating vortices. More precisions on the flow topology can
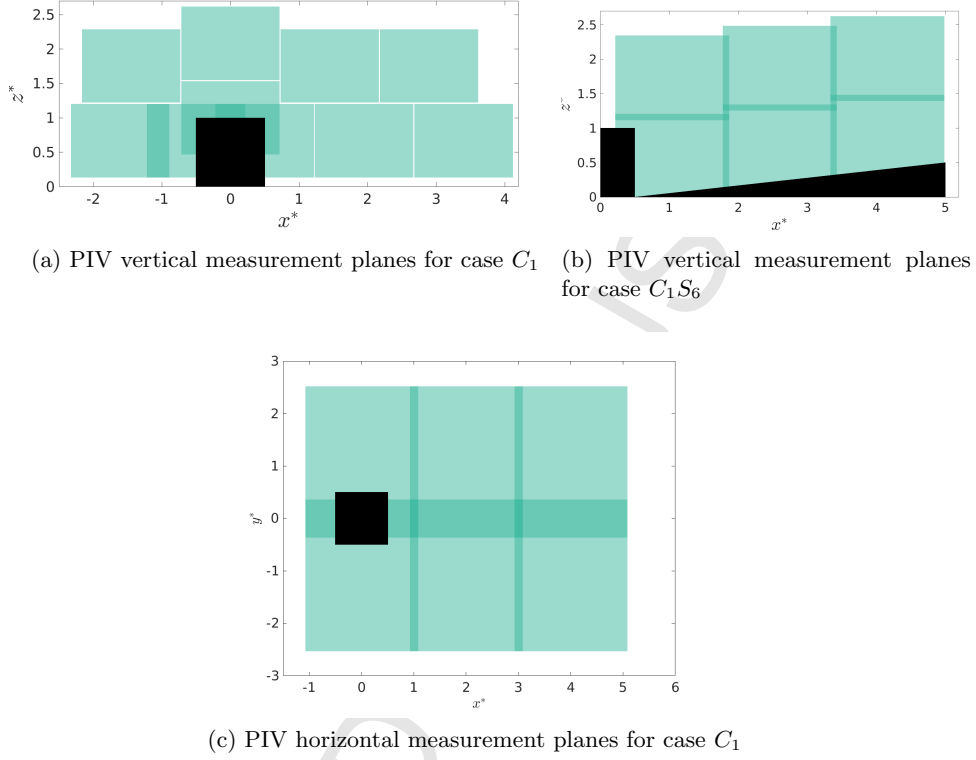
7

(a) PIV vertical measurement planes for case C_1

(b) PIV vertical measurement planes for case C_1S_6

(c) PIV horizontal measurement planes for case C_1

Figure 5: Representation of vertical measurement planes with a resolution of 1600pix $\times$ 1200pix and a precision in term of pixel size for vertical planes of $0.43mm$ and for horizontal planes of $0.21mm$ for case C_1 and $0.25mm$ for case C_1S_6

be found in [12].

3.2. Inclined floor effects

An inclined floor is added downstream of the cube (case C_1S_6). PIV measurements show that the aspect of the wake is strongly influenced by the presence of the floor as can be seen on the streamlines maps (see fig.8) and the $\overline{W}$ maps (see fig.9). $\overline{W}$ maps clearly show a strong area where $\overline{W} < 0$ for case C_1 illustrating the flow going towards the floor on the outline of the recirculation region whereas case C_1S_6 shows a small area where $\overline{W} < 0$ at top of the recirculation region and the rest of the flow shows a reduced area where $\overline{W} > 0$. These maps illustrate the fundamental wake
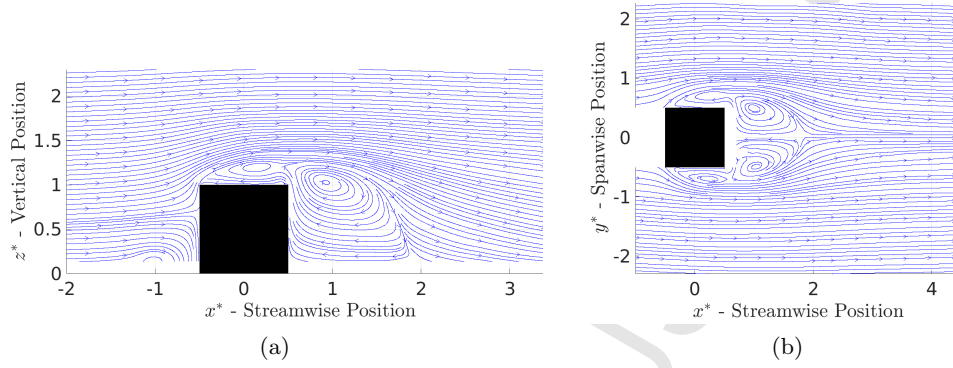
8

Figure 6: Streamlines for case C_1. Left hand side: vertical PIV measurements, at the median plane $y^* = 0$. Right hand side: horizontal PIV measurements, at an altitude of $z^* = 0.7$. White parts indicate areas where measurements were no measures are performed or where the laser light was not sufficient. $l^*_{us} = 0.7$, $l^*_{top} = 0.4$, $l^*_{ds} = 1.9$ and $z_{st}* = 0.7$.
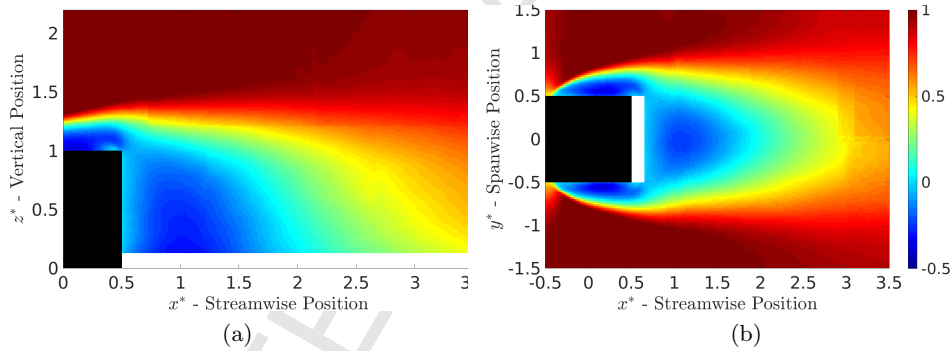

Figure 7: $\overline{U}/U_\infty$ (with $U_\infty = 1\ m/s$) maps for case C_1 using PIV measurements. Left hand side: vertical view. Right hand side: horizontal view.

differences between both cases: for C_1, the flow is oriented towards the floor and for $C_1 S_6$ it is rather directed towards the water surface.

However, the main characteristics of the recirculation region stay the same: the centre C remains at the same location behind the cube ($x^* = 0.9$, $z^* = 1$). The effects of the floor start appearing further downstream. The main difference is the appearance of a stagnation point S at ($x^* = 1.7$, $z^* = 0.7$) located on the outline of the recirculation region (fig. 8(b)). The appearance of this stagnation point S can be caused by the flow passing over and by the sides of the cube. Side vortices are impulsed in altitude by the inclined

9

floor and they interact with the top vortex leading to the appearance of a stagnation point. The streamlines plotted in figure 8 illustrate the shortening of the recirculation region : $l_{ds}^*(C_1S_6) = 1.7$ compared to $l_{ds}^*(C_1) = 1.9$.
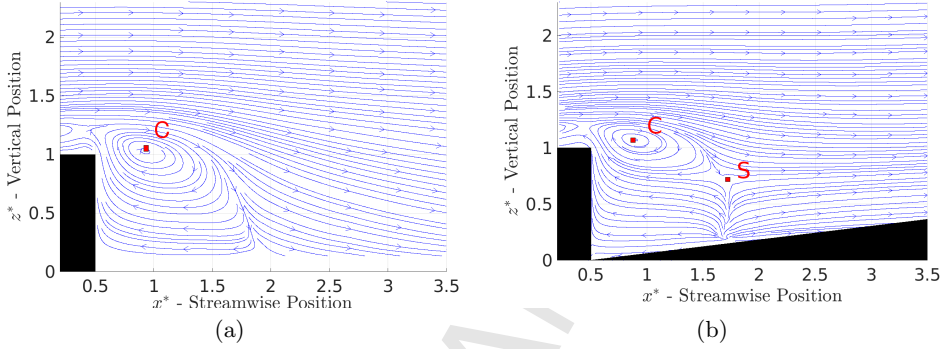

Figure 8: Streamlines using PIV vertical measurements at median plane ($y^* = 0$). Left hand side: case C_1. Right hand side: case C_1S_6. C the recirculation zone centre and S the stagnation point.
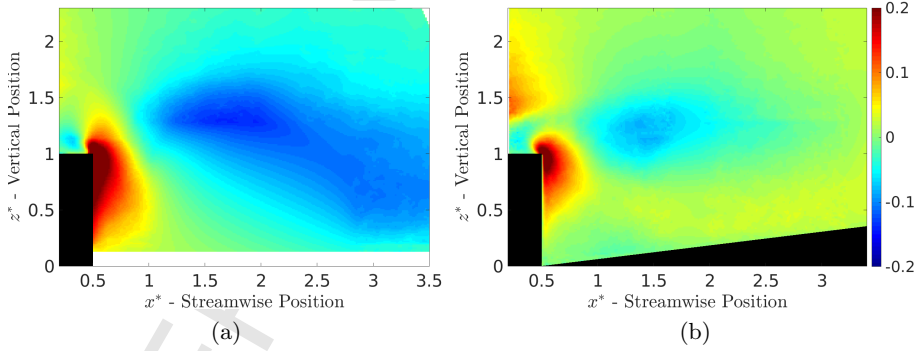

Figure 9: $\overline{W}/U_\infty$ (with $U_\infty = 1\ m/s$) maps for cases C_1 and C_1S_6 using PIV measurements. Left hand side: case C_1. Right hand side: case C_1S_6.

In figure 10, τ_{uw} maps give a good visualisation of the shear layer that develops between the outer undisturbed flow and the recirculation zone. The shear layer formation still occurs at the edges of the obstacle where fluid separation takes place. However, downstream, the inclined floor squeezes it. The shear layer is then thinner for case C_1S_6. Figure 10 also illustrates the

10

shortening of the shear layer with the inclined floor: at $x^* = 3.5$, the shear is strongly reduced for case $C_1 S_6$ and still persists for case C_1. Finally, the impulsion of the floor inclination reorientates the shear layer towards the surface and it reaches higher altitude in case $C_1 S_6$.
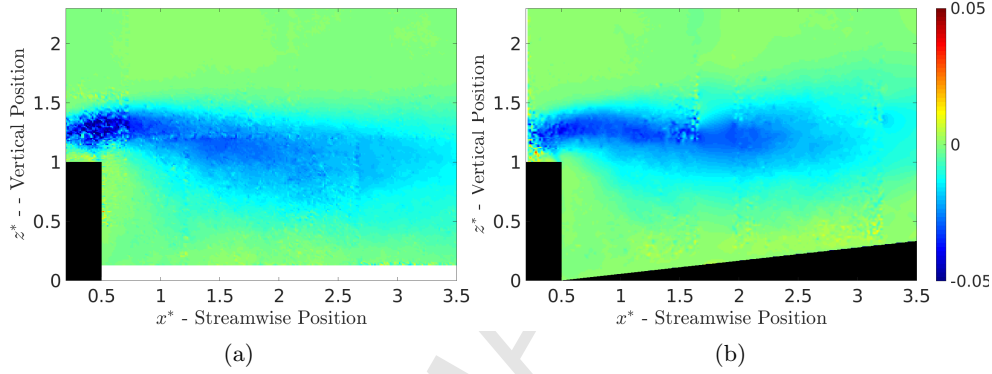

Figure 10: τ_{uw}/U_∞^2 (with $U_\infty = 1\ m/s$) maps using PIV vertical measurements ($y^* = 0$). Left hand side: case C_1. Right hand side: case $C_1 S_6$.

To evaluate the effect of the inclined floor on the flow development, the streamwise growth rate of the shear layer is estimated in the $y^* = 0$ plan for both cases. First, the centre (z_0) of the shear layer is determined for each streamwise position. It corresponds to the inflexion point of the mean velocity profile. Second, in each streamwise position x, the vorticity thickness is computed:

$$\delta_w(x) = \frac{U_s}{(dU_s/dz)_{z=z_0}} \qquad (2)$$

where $U_s = U_\infty - U_i(x)$ with $U_i(x)$ the streamwise velocity underneath the shear layer.

In order to find the inflection point, for each streamwise position x, $U_s(x, z)$ is fitted by a function $f(x, z) = a(x) + b(x)\tanh(c(x)z)$. Results are presented in figure 11 for both cases. The δ_w graph shows that the shear layer is thinner for case $C_1 S_6$, confirming the squeezing effect mentioned earlier. The vorticity thickness difference between both test cases starts at 0 at the trailing edge of the cube and then increases until $x^* = 1$. Then the difference remains constant at $\Delta\delta_w = 0.08$. The inclined floor effect is strong where the shear layer originates and then reduced. The streamwise evolution

11

of z_0^* illustrates the rise of the shear layer in case $C_1 S_6$ contrarily to case C_1. The shear layer centre evolution follows the inclined plane translation until $x^* = 2.5$. Downstream of that position, the flow becomes more turbulent avoiding any well determination of the $U_i(x)$ velocity component.
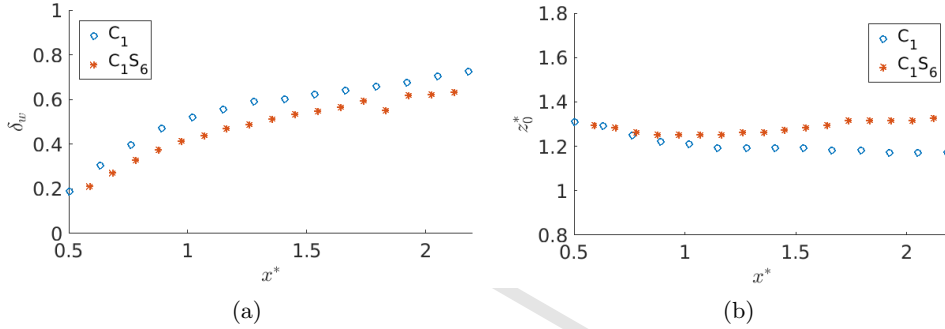

Figure 11: Left hand side: streamiwse evolution of the vorticity thickness δ_w. Right hand side: streamwise evolution of the z_0 shear layer centre; for case C_1 ($\circ$) and $C_1 S_6$ (*)

In order to have a more quantitative comparison in the downstream region, two streamwise positions are chosen at: $x^* = 2.5$ and $x^* = 3.6$. These positions are selected to avoid any recovering issues of the different PIV measurement planes. For case C_1, profiles are measured from $z^* = 0.2$ and for case $C_1 S_6$, from the altitude of the floor. The profiles of $\overline{U}$, τ_{uw} and k_{uw} are plotted along the Z axis in figure 12 and 13. The profiles at $x^* = 1$ are similar for both test cases and are not represented here. However, at $x^* = 2.5$ the floor impact begins to be well pronounced.

The shear layer (although thinner) reaches higher positions when impulsed: the τ_{uw} peak at $x^* = 2.5$ is translated $\Delta z^* = 0.23$ higher for case $C_1 S_6$. It is around the elevation of the inclined floor at this position ($z^*_{floor} = 0.28$). The peak shows a simple translation of the τ_{uw} profiles. Furthermore at $x^* = 2.5$, the peak intensity is about 10% more intense for case $C_1 S_6$ indicating a stronger shear. At $x^* = 3.6$, however, the shear peak is as intense for case C_1 as for case $C_1 S_6$. This confirms what can be visualized on the maps in figure 10: the shear layer dissipates faster and shortens for case $C_1 S_6$. It is expected that, consequently, the wake will be shorter as well.

The $\overline{U}$ profiles show that as long as we are above the shear layer ($z^* > 0.5$ for $x^* = 2.5$ and $z^* > 1.1$ for $x^* = 3.6$), $\overline{U}(C_1 S_6) > \overline{U}(C_1)$. Underneath the shear layer, the impulsion of the floor causes an increase of $\overline{W}$ (see figure 9) that reduces $\overline{U}$. Above the shear layer, for $z^* > 2.2$, for both streamwise

12

positions, τ_{uw} (and $\overline{U}$) profiles meet at $\tau_{uw} = 0$ ($\overline{U} = 1$ resp.) and the floor impact is no longer visible. The only difference between cases C_1 and C_1S_6 at higher altitude appears on the k_{uw} profiles. In figure 13(a), for $x^* = 3.6$, $k_{uw}(C_1S_6) > k_{uw}(C_1)$ until the highest location measured ($z^* = 2.3$). This 2D turbulent kinetic energy persists until higher location than the simple translation ($z^*_{floor} = 0.4$ at $x^* = 3.6$) given by the inclined floor, as can be observed on the τ_{uw} profiles. For a better understanding, the k_{uw} profile for case C_1 is translated of $z^*_{floor} = 0.4$ in figure 13(b). It shows that, additionally to the translation, k_{uw} is still 50% higher for case C_1S_6 at $z^* = 2$. 2D turbulent kinetic energy rises substantially with the addition of the inclined floor.
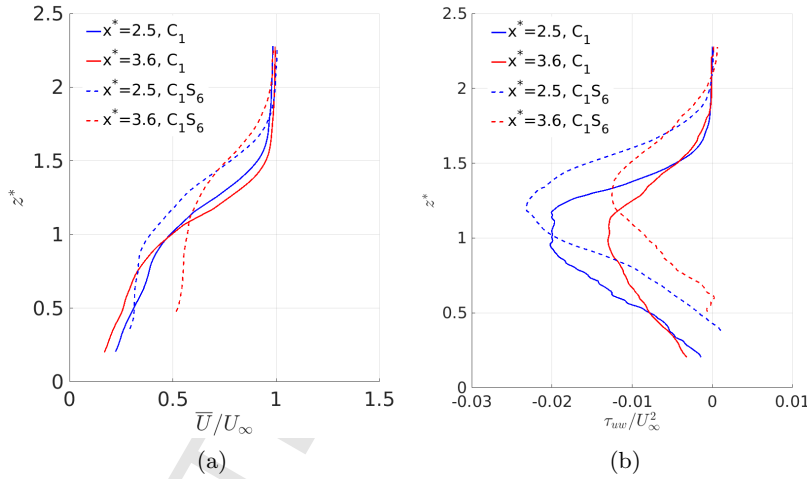

(a)   (b)

Figure 12: $\overline{U}/U_\infty$ and k_{uw}/U_∞^2 profiles comparison cases C_1 ($-$) and C_1S_6 ($--$) at $x^* = 2.5$ and $x^* = 3.6$, $y^* = 0$ and along the Z axis.

4. Application of the Proper Orthogonal Decomposition coupled with the quadrant method

In this part, POD is used as a filter in order to select the highest energetic structures and leave aside the non-coherent turbulent part. Then, based on the extracted energetic flow structures, the quadrant method is implemented to try to elucidate the turbulent events present in the flow.
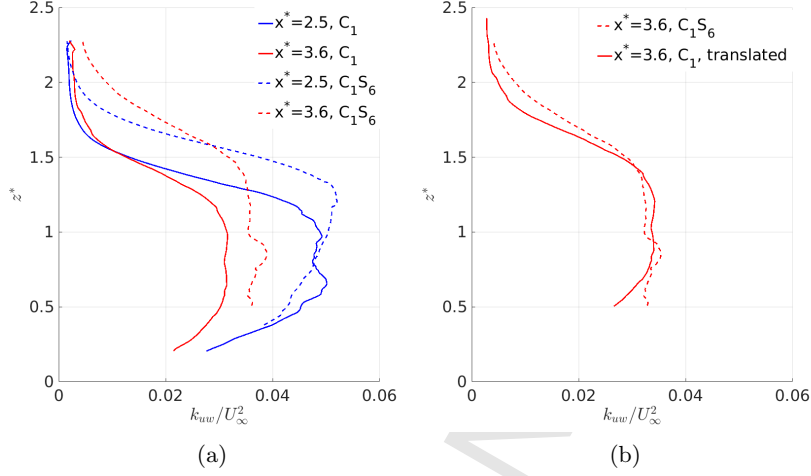
13

Figure 13: Left hand side: k_{uw}/U_∞^2 profiles at $x^* = 2.5$ and $x^* = 3.6$. Right hand side: k_{uw} profiles at $x^* = 3.6$. Case C_1 is translated from $\Delta z^* = 0.4$ (altitude of the $6.5°$ inclined floor at $x^* = 3.6$). Profiles comparison cases C_1 $(-)$ and $C_1 S_6$ $(--)$ at $y^* = 0$ and along the Z axis.

After a brief description of the mathematical concept of POD and the quadrant method, the POD analysis of the PIV velocity fields is examined. Then, the results based on the application of the quadrant method to the POD extracted velocity field are discussed.

4.1. Brief Mathematical description of POD

First introduced by Lumley [13], POD is an efficient and optimal mathematical tool to extract energetic coherent structures embedded in a turbulent flow. In this context, a coherent structure is the structure that has the largest mean square projection of the velocity field. Mathematically, it corresponds to the determination of a basis which is optimal in an energetic sense. It consists of searching a function $\phi(\mathbf{X})$ which maximizes in a mean square sense the projection of the instantaneous fluctuating velocity field on $\phi(\mathbf{X})$. These functions are then the solution of the Fredholm equation:

$$\sum_{j=1}^{N_c} R_{ij}(\mathbf{X}, \mathbf{X}')\phi_j^{(n)}(\mathbf{X}')d\mathbf{X}' = \lambda^{(n)}\phi_i^{(n)}(\mathbf{X}) \tag{3}$$

where $R_{ij}(\mathbf{X}, \mathbf{X}') = \overline{u_i'(\mathbf{X})u_j'(\mathbf{X}')}$ is the time-averaged two-point spatial correlation tension, N_c is the number of velocity components considered.
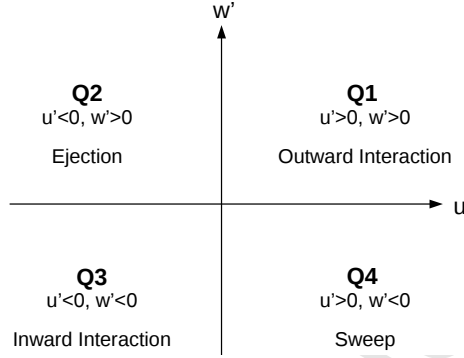
14

Figure 14: Schematic representation of quadrant decomposition

$\phi^{(n)}$ represents the nth eigenfunction and $\lambda^{(n)}$ the nth eigenvalue of the correlation tensor. The POD modes are orthogonal and each fluctuating velocity component can thus be represented by a linear combination of deterministic modes as follows:

$$u_i'(\mathbf{X}, t) = \sum_{n=1}^{N_{POD}} a^{(n)}(t) \phi_i^{(n)}(\mathbf{X}) \qquad (4)$$

Coefficients $a^{(n)}(t)$ are determined through the projection of the velocity field onto $\phi^{(n)}$ and are mutually orthogonal and uncorrelated. The previous part describes the classical POD method proposed by Lumley [13]. The snapshot version of POD [22] is used in the present work.

Details of the implementation of POD technique applied to PIV database can be found in [8] and [7]. Such an application allows the extraction of energetic flow structures embedded in the turbulent flow. A annual review, made by Wallace [24] explains that quadrant analysis is pertinent preceded by POD. Then following previous works [5, 19], the resulted POD filtering velocity field is used for the next quadrant analysis to investigate the nature of the extracted organized flow structures.

4.2. Brief description of the quadrant method

Quadrant analysis is a way of characterizing energetic event in a turbulent flow not only in turbulent boundary layer flow [1] but also in turbulent flow developing over dunes [2]. It separates each $u'w'$ event into four categories called quadrants as illustrated in figure 14. Q1 ($u' > 0$, $w' > 0$) represent outward interactions of fluid (outward motion of high-momentum

15

fluid), Q2 ($u' < 0$, $w' > 0$) events are ejections of low-momentum fluid from the shear layer, Q3 ($u' < 0$, $w' < 0$) contain inward interaction of fluid (inward motion of low-momentum fluid) and finally, Q4 ($u' > 0$, $w' < 0$) contain sweep of high-momentum fluid towards the wall. Q2 and Q4 events are associated elements. They correspond to the largest contribution to the Reynolds shear stress [2, 24]. In the present study, a shear layer is formed due to the presence of the cube and turbulent structures are shed from the layer. It is then expected that the application of quadrant method allows the extraction of events that are emitted from the shear layer.

4.3. POD analysis of PIV measurement fields

Choice of a common area.

Following previous work [2] and to avoid any measurement plane overlap, a common area is retained. The location of this area illustrated in figure 16(a) is defined as follows: $x^* \in [2.2; 3.2]$ and $z^* \in [1.5; 2.2]$. The choice of $z^* = 1.5$ is meant to look above the shear layer, between the shear layer and the outer flow. The spatial area contains $(n_x \times n_y) = (68 \times 47) = 3196$ measurements points for case C_1 and $(n_x \times n_y) = (59 \times 42) = 2478$ for case $C_1 S_6$.

POD application.

First, the fluctuating part of each instantaneous velocity field is determined thanks to the Reynolds decomposition. Second, in each test case, the vectorial POD is performed from the two available fluctuating velocity components leading to obtain $N_{POD} = N_{acqu} = 2250$ modes. Figure 16(b) displays the cumulative energy content for the first 100 modes for both test cases. POD energy repartition differs from both cases. $C_1 S_6$ reaches higher energy level faster than case C_1. This shows that more energetic organized flow structures are present in the $C_1 S_6$ flow configuration. Case C_1 exhibits less organized energetic structures in the common observation window. In each test case, instantaneous velocity vectors are then projected onto the first N_i POD modes (with $i = C_1$ or $C_1 S_6$) as follows:

$$u'^{POD}(\mathbf{X}, t) = \sum_{n=1}^{N_i} a^{(n)}(t)\phi_u^{(n)}(\mathbf{X}) \text{ and } w'^{POD}(\mathbf{X}, t) = \sum_{n=1}^{N_i} a^{(n)}(t)\phi_w^{(n)}(\mathbf{X})$$
(5)

N_i which is function of the flow configuration has to be firstly determined. For such an investigation, the quadrant analysis will be conducted. Beforehand, as the energy level of the u' component is higher than the one

16

of w', the resulted $\phi_w^{(n)}(\mathbf{X})$ POD modes may be questionable. To avoid any ambiguity, a preliminary analysis is done. Two scalar PODs are separately performed on u' and w', and results are compared to the vectorial POD results. Spatial shape $\sqrt{\lambda^{(n)}}\phi_w^{(n)}(\mathbf{X})$ of the firsts 6 modes is presented for scalar POD (top) on w' and vectorial POD (bottom) in figure 15 for case C_1S_6 on the common plane. In a similar way, comparative analysis of the spatial POD modes $\sqrt{\lambda^{(n)}}\phi_u^{(n)}(\mathbf{X})$ was performed and again for both velocity components for C_1 case. For each mode and each component, the order of magnitude and global aspect of the spatial modes are the same. Furthermore, the next following analyses have been done from scalar POD results and similar results are obtained.

A point is randomly chosen in the common plane ($\mathbf{X}_D = (x_D^* = 3, z_D^* = 1.6)$), where $u'^{POD}(\mathbf{X}_D, t)$ and $w'^{POD}(\mathbf{X}_D, t)$ are successively determined with varying N_i number. In the graph, N_i is the number of POD modes considered for case i ($i = C_1$ or $i = C_1S_6$), see equation 5. The study was also carried out for other points and for both cases. Based on these velocity signals, the quadrant method is performed and the study of the impact of the number of POD modes on the quadrant proportion is achieved in figure 17 in $\mathbf{X}_D$ for both C_1 and C_1S_6. It appears that, above $N_i = 6$, the quadrant repartition achieves a certain modes number independence. It would not be necessary to use more modes for this study. Hence 6 modes are chosen for case C_1S_6, looking at figure 16(b), it appears that 6 modes represent 45% of energy for case C_1S_6. In order to have to same energy content, 9 modes are chosen for case C_1 to reach 45% of energy. Hence, the fluctuating flow field is recomposed using $N_{C_1} = 9$ modes and $N_{C_1S_6} = 6$ respectively (see equations 5). The number of modes chosen for the study is higher for case C_1. Figure 17 also shows that Q2 and Q4 are substantially more present for case C_1S_6 than for case C_1 at the location D.

Q2/Q4 events predominance for case C_1S_6 is consistent with the lower number of POD modes N_i required that indicates more organized structures.

Quadrant method application.
Each turbulent velocity pair may be investigated either through examination of the entire signal (like [19] and [5] and our previous study) or only with $u'w'$ events that lie above a certain threshold value (H_t) (like [2]) defined in equation 6:

$$|u'^{POD}w'^{POD}| \geq H_t \times |\overline{u'^{POD}w'^{POD}}| \tag{6}$$
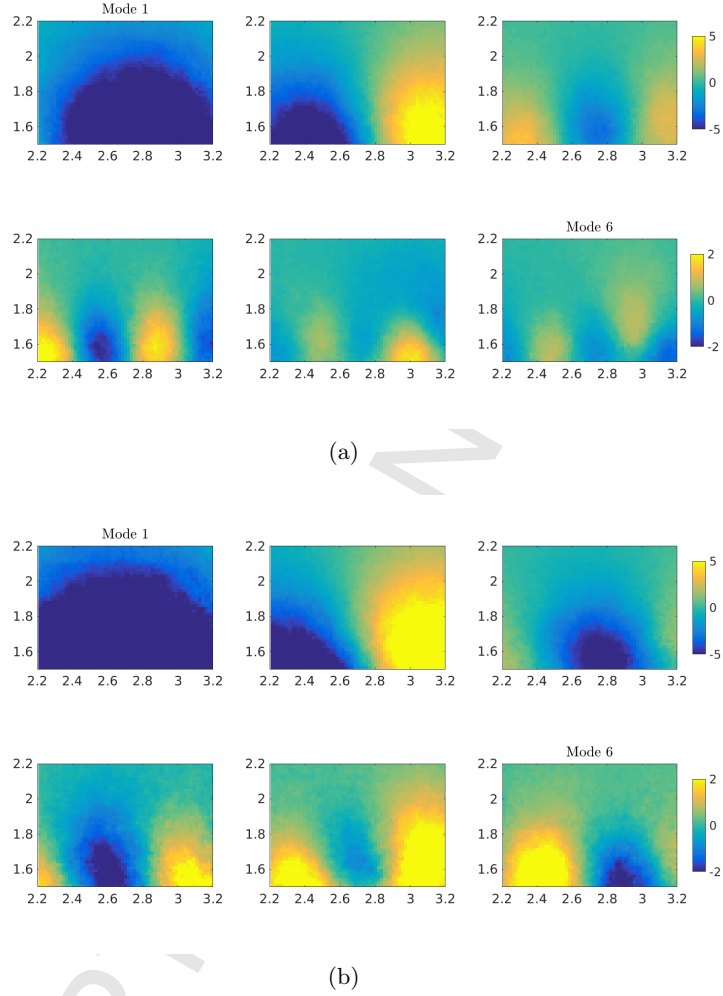
(a)

(b)

Figure 15: Spatial modes $\sqrt{\lambda^{(n)}}\phi_w^{(n)}(\mathbf{X})$ of w' with $n \in [1; 6]$ the mode number using scalar POD (top) and vectorial POD (bottom) for case $C_1 S_6$, plane 4. Colormaps are different for modes 1,2,3 and modes 4,5,6.

The impact of the quadrant proportions versus H_t is studied in figure 18 from instantaneous POD filtering velocity field extracted at the point D defined above and point B with $\mathbf{X}_B = (x_B^* = 3, z_B^* = 2.1)$ and for case $C_1 S_6$ where quadrant differences are the more significant. Of course, the larger the H_t value, the lower the quadrants proportion. For point B (figure 18(a)), at $H_t = 0$, Q3 is more present. However, as soon as $H_t > 0.1$, the predominance

18
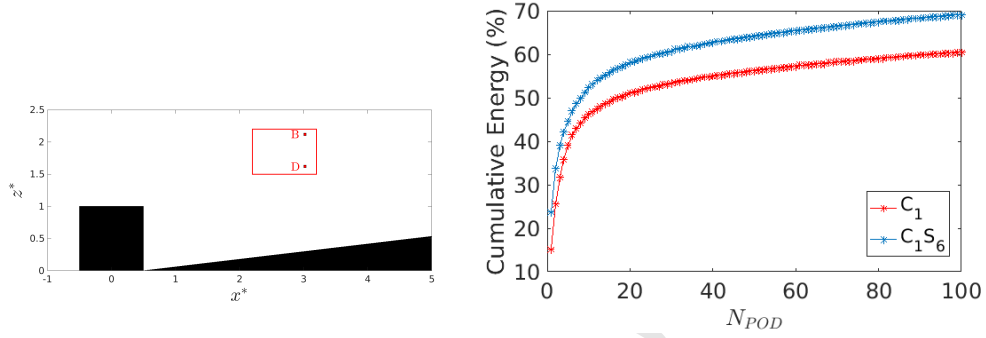
(a) Observation window for POD, common to case C_1 and C_1S_6: $x^* \in (2.2; 3.2)$ and $z^* \in (1.5; 2.2)$ with B and D specific points for the study

(b) Cumulated energy of each POD modes on the common plane for cases C_1 and C_1S_6

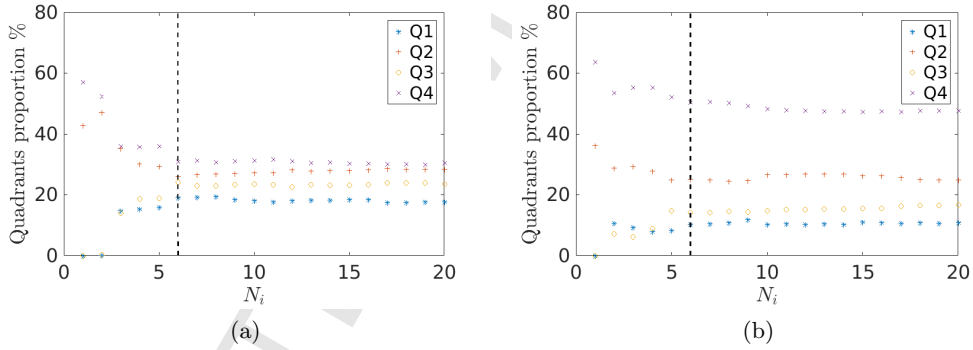Figure 16: POD applied on a common plane for cases C_1 and C_1S_6

(a)

(b)

Figure 17: Left hand side: case C_1. Right hand side: case C_1S_6. Evolution of the quadrant proportion as a function of N_i values. Quadrants proportion (%) are computed from POD filtered fields using different N_i values (see equation 5) and extracted at point $D = (x_D^* = 3, z_D^* = 1.6)$ for both cases. Dotted line indicates $N_i = 6$

disappears and results show all quadrants in similar proportions (between 10 and 15%). This shows that what appeared to be a Q3 predominance, when slightly filtered shows an even distribution between quadrants. For point D (figure 18(b)), the study shows that for low filtering ($H_t < 0.5$), Q4 is predominant. However, for higher values ($H_t > 1$), Q2 is more present in point D. It shows that Q2 events dominate the flow, however Q4 events are the most energetic events even if they are in lower proportion.
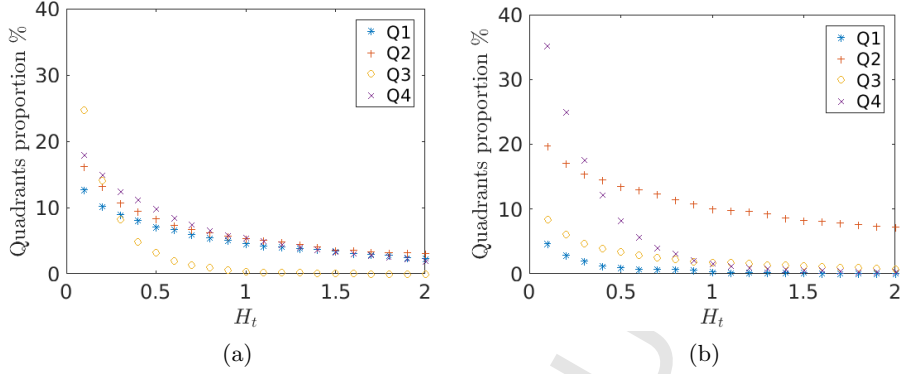
19

Figure 18: Quadrants proportion (%) versus H_t in $\mathbf{X}_B = (x_B^* = 3, z_B^* = 2.1)$ (Left hand side) and $\mathbf{X}_D = (x_D^* = 3, z_D^* = 1.6)$ (Right hand side). Case C_1S_6, $N_{C_1S_6} = 6$.

In this study, filtering is achieved with POD. Adding a criteria on H_t would add a second filter that is not useful for the comparison here, hence the choice of $H_t = 0$ is retained. However, figure 18 allows to understand the energy repartition between Q2 and Q4 events.

4.4. Results of coupled POD-quadrant analysis

The method described in this section (POD + quadrant, with $H_t = 0$) is now applied on every point of the common window for both cases. Results are presented in figure 19 with the repartition of the quadrant events in the window.

Results show a clear increase of Q4 events for case C_1S_6. Furthermore, the rise of these events is all the more intense when they are impulsed. This analysis justifies the assumption made that, with the presence of an inclined plane, turbulent structures are emitted higher and with a stronger intensity away from the shear layer. It is worth noting that at $x^* = 2.2$, the inclined floor is at $z^* = 0.25$ and for $x^* = 3.2$, at $z^* = 0.36$. It is clear that Q4 events rise higher than the simple impulsion given by the inclined floor. As mentioned in previous section, Q2 events do not appear in figure 19 because they are less present as Q4 but they exist in lower proportion and with a high intensity. Case C_1S_6 also shows a light increase of Q3 events for $z^* > 2$. As explained in previous paragraph, looking at point B that lies in this area, when increasing $H_t > 0.1$, all events are in similar proportions (see figure 18(a)).

20
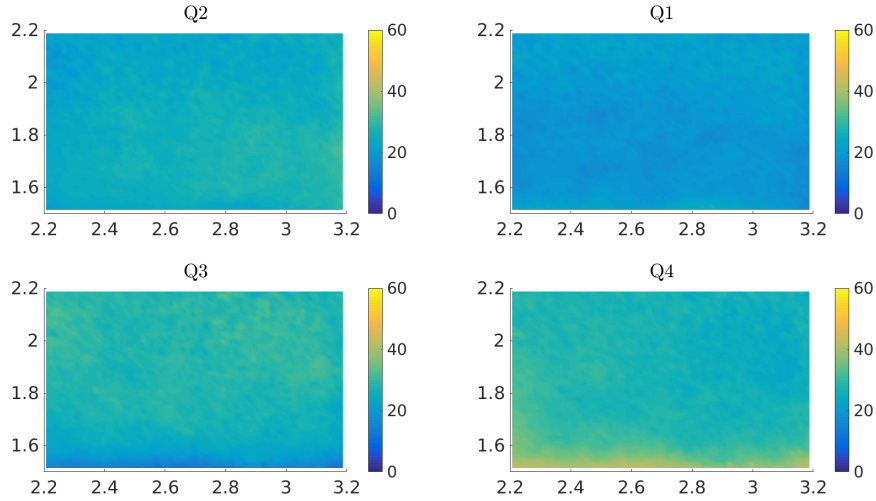
(a)
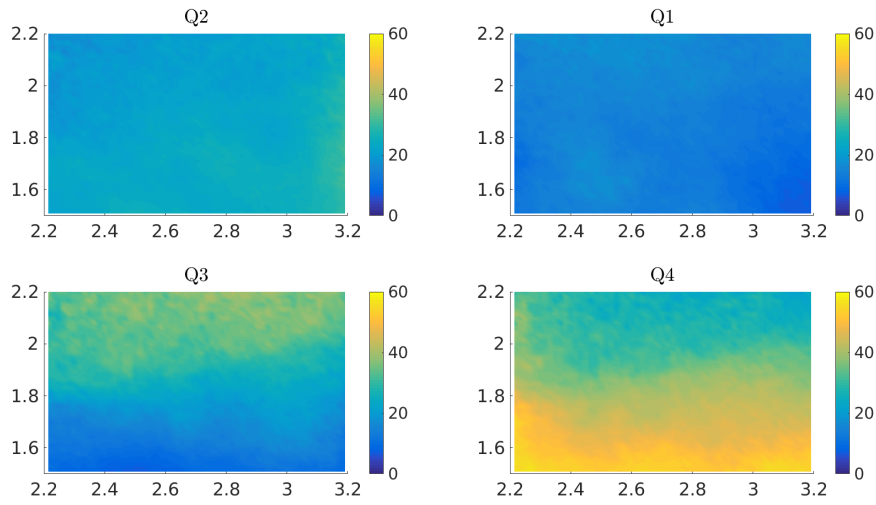
(b)

Figure 19: Top: case C_1, $N_{C_1} = 9$. Bottom: case $C_1 S_6$, $N_{C_1 S_6} = 6$. Quadrants proportion (%) in the whole common plane for both cases.

For a more quantified comparison, profiles are plotted against the alti-

21

tude at $x^* = 3$ in figure 20. For case C_1 and $z^* < 1.6$, Q4 is the more present event. However, higher in the water column, all the events are in even proportions (between 20 and 30%). For case C_1S_6, as observed earlier, strong predominance of Q4 event is seen for $z^* < 2$. Higher in the flow, events are in similar proportion (between 18 and 35%). It is assumed that, higher in the water column ($z^* > 2.2$), even quadrant repartition is achieved. Even quadrant proportion indicates that no energetic structures (sweep or ejections) is detected hence the equipartition of all events. It is the outer flow where the obstacle no longer have influence.
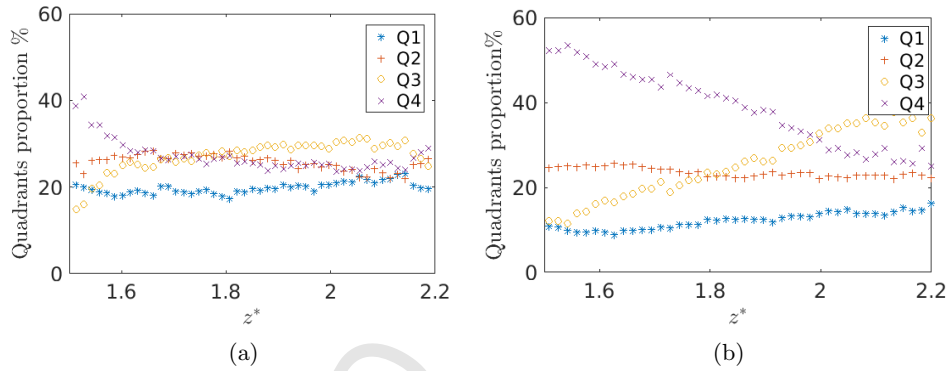

Figure 20: Left hand side: case C_1, $N_{C_1} = 9$. Right hand side: case C_1S_6, $N_{C_1S_6} = 6$. Quadrants proportion (%) at $x^* = 3$ against altitude z^*.

Results are schematically represented in figure 21. Using figure 19 and profiles in figure 20, the Q4 area of predominance is determined in the chosen observation window. The rise of the cube influence due to the inclined floor presence is represented.

To summarize, we use a POD filter and look at the different Reynolds-shear stress events with the quadrant method. With a proper choice of POD modes number, quadrants proportion can be evaluated on a map for both cases. Q2 and Q4 events are known to be the main contributors to Reynolds shear stress. It is shown in this study that these events are stronger and rise higher in the water column for case C_1S_6 compared to case C_1.
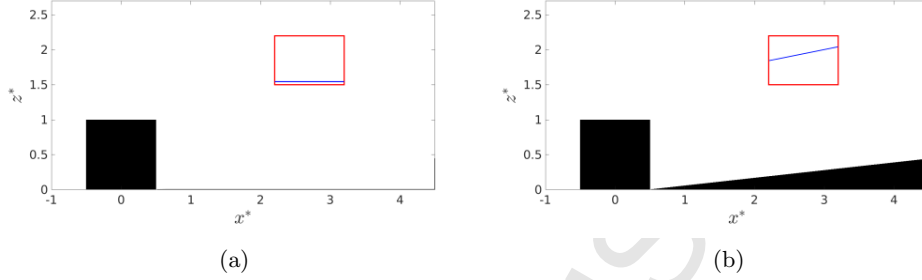
22

Figure 21: Left hand side: case C_1. Right hand side: case $C_1 S_6$. Schematic representation of the extend of the obstacle influence using POD analysis and selecting Q4 predominance area

5. Conclusion & Perspectives

In this study, the flow past elements representative of the seabed is described. The rise of turbulent structures and the behaviour of the shear layer are studied. First set of experiments on the wall-mounted cube in a low turbulence intensity flow show similar results to those found in the literature for lower Reynolds number with regards to the flow topology (like the recirculation length, $l_{ds}^* = 1.9$).

In order to understand the impact of the floor inclination on the obstacle wake, an inclined floor is added downstream of the cube. Consequently, to have a flow rate conservation, the average streamwise velocity increases with the addition of the floor. The recirculation zone reduces from $l_{ds}^* = 1.9$ to $l_{ds}^* = 1.7$ and a stagnation point S appears. The shear layer becomes shorter and thinner. However, the Reynolds shear stress, at its maximal value is more intense: 10% stronger at $x^* = 2.5$. It is assumed that due to the squeezing effect, the shear is stronger indicating a better mixing. Then, the greater the mixing, the faster the wake dissipation. Hence the wake shortens. It is also observed that, above $z^* = 2.2$, in spite of the inclined floor translation, the 2D turbulent kinetic energy is stronger for the case with inclined floor. This indicates stronger fluctuating velocities. It is assumed that the presence of a stagnation point above the floor increases the emission of turbulent structures that reach high altitudes in the water column. A POD analysis is carried out and instantaneous velocity vectors are projected onto the first six (for $C_1 S_6$) and nine (for C_1) energetic modes to reach 45% of energy level. The resulted POD filtered velocity fields are

23

used as input data for a quadrant analysis. Results show a more intense presence of Q4 events for case C_1S_6 on a chosen observation window. Q2 events are also present in a lower proportion but with a higher energetic level.

This study showed the strong impact of an inclined floor downstream of a wall-mounted cube in a high-Reynolds number incoming flow. The inclined floor, does not only translated the obstacle wake, it is the source of a stronger emission of sweep and ejection events that are highly energetic. The major conclusion is that these event are stronger for case C_1S_6 and they are expected to rise substantially higher in the water column, more than the simple impulsion given by the floor altitude variations.
The results of this study are meant to explain real-life phenomenon observed at sea, the goal being to understand the turbulence generated at the sea bottom in the Alderney Race. The cube is representative of the mean bathymetric variation of this area and the inclined floor of a smooth depth variation. When choosing an area for marine current turbines, one must consider the presence of seabed elevation or not (*i.e.* presence of an inclined floor or not). Shear layer presence and energetic events may have an impact on the turbine and blade fatigue, hence floor elevation need to be considered and a specific study on the seabed topology might be required.

In this study, the measurements are limited to the near wake of the obstacle in order to properly study the impact of the obstacle on the flow. Measurements in the far wake are then required and PIV measurements seem to be appropriate for that purpose even if the obstacles considered here remain simple cases that are too canonical to reproduce real life turbulent structures. After studying each individually, a combination of several cubes, wide cylinder and the inclined floor will be investigated. Then, the effect of this kind of turbulent structures on the behaviour of a tidal turbine will be investigated. A turbulence intensity closer to real-life conditions ($I = 15\%$) is achievable in the tank, the impact of the incoming turbulence intensity on obstacles wake is another possible development. Upstream turbulence intensity impact on the wake of a cube is already studied in the literature and the present study offers the understanding of the effect of the addition of an inclined floor on the wake. Combining both could also be investigated.

Acknowledgement

Nomenclature

Dimensional quantities:

D	Depth	m
δ_w	Shear layer thickness	m
f_e	Sampling frequency	H_z
H	Cube height	m
l_{ds}	Downstream recirculation length	m
l_{top}	Top of the cube recirculation length	m
l_{us}	Upstream recirculation length	m
$\overline{U}$	Average streamwise velocity	m/s
u'	Fluctuating streamwise velocity	m/s
u'^{POD}	POD filtered, fluctuating streamwise velocity	m/s
$\overline{V}$	Average spanwise velocity	m/s
v'	Fluctuating spanwise velocity	m/s
v'^{POD}	POD filtered, fluctuating spanwise velocity	m/s
$\overline{W}$	Average vertical velocity	m/s
w'	Fluctuating vertical velocity	m/s
w'^{POD}	POD filtered, fluctuating vertical velocity	m/s
z_0	Shear layer centre altitude	m
z_{st}	Stagnation point altitude	m

Non dimensional quantities:
(Quantities stated with a * are length reduced by H, for instance: $x^* = x/H$)

H_t	Threshold value for quadrant method
k_{uw}	2D turbulence kinetic energy
N_{acqu}	Number of temporal sample
N_{POD}	Total modes number for snapshot POD
N_{C_1}	Modes number selected for analysis for case C_1
$N_{C_1 S_6}$	Modes number selected for analysis for case $C_1 S_6$
n_x	Spatial sample in the horizontal direction
n_y	Spatial sample in the vertical direction
R_e	Reynolds number
F_r	Froude number
I	Turbulence intensity
S_t	Strouhal number
τ_{uw}	Averaged Reynolds shear stress

References

[1] R.J. Adrian, C.D. Meinhart, and C.D. Tomkins. Vortex organization in the outer region of the turbulent boundary layer. *J. Fluid. Mech*, 422:1–54, 2000.

[2] S.J. Bennet and J.L. Best. Mean flow and turbulence structure over fixed, two-dimensional dunes: implications for sediment transport and bedform stability. *Sedimentology*, 42:491–513, 1995.

26

[3] J. Best. The fluid dynamics of river dunes: A review and some future research directions. *J. Geophys. Res.*, 110, 2005.

[4] A. Bourgoin, S. Guillou, J. Thiébot, R. Ata, and S. Benhamadouche. Development of a large-scale eddy simulation approach for tidal currents modelling. *EWTEC*, 2017.

[5] W.H. Cai, F.C Li, H.N. Zhang, X.B. Li, X.B. Yu, J.J. Wei, Y. Kawaguchi, and K. Hishida. Study on the characteristics of turbulent drag-reduction channel flow by particle image velocimetry combining with proper orthogonal decomposition analysis. *Phys. Fluids*, 21:115103, 2009.

[6] I.P. Castro and A.G. Robins. The flow around a surface-mounted cube in uniform and turbulent streams. *J. Fluid Mech.*, 79:307–335, 1977.

[7] Ph. Druault, E. Bouhoubeiny, and G. Germain. Pod investigation of the unsteady turbulent boudary layer developing over porous moving flexible fishing net structure. *Exp. Fluids*, 53:277–292, 2012.

[8] Ph. Druault, P. Guibert, and F. Alizon. Use of proper orthogonal decomposition for time interpolation from PIV data. application to the cycle-to-cycle variation analysis of in-cylinder engine flows. *Exp. Fluids*, 39:1009–1023, 2005.

[9] O. Duràn Medina, F.G. Schmitt, R. Calif, G. Germain, and B. Gaurier. Turbulence analysis and multiscale correlations between synchronized flow velocity and marine turbine power production. *Renew. Energ.*, 112:314–327, 2017.

[10] R. Jason Hearst, G. Gomit, and B. Ganapathisubramani. Effect of turbulence on the wake of a wall-mounted cube. *J. Fluid Mech.*, 804:513–530, 2016.

[11] H.J. Hussein and R.J. Martinuzzi. Energy balance for turbulent flow around a surface mounted cube placed in a channel. *Phys. Fluids*, 8:764–780, 1996.

[12] M. Ikhennicheu, Ph. Druault, B. Gaurier, and G. Germain. An experimental study of influence of bathymetry on turbulence at a tidal stream site. *EWTEC*, 2017.

[13] J.L. Lumley. The structure of inhomogeneous turbulent flows. *A.M. Yaglom, V.I. Tararsky (Eds.), Atmospheric Turbulence and Radio Wave Propagation*, 1967.

[14] R. Martinuzzi and C. Tropea. The flow around surface-mounted, prismatic obstacles placed in a fully developed channel flow, *(Data Bank Contribution)*. *J. Fluid Eng.*, 115:85–92, 1993.

[15] D. McArthur, D. Burton, M. Thompson, and J. Sheridan. On the near wake of a simplified heavy vehicle. *J. Fluid. Structs.*, 66:293–314, 2016.

[16] C.D. Meinhart, A.K. Prasad, and R.J. Adrian. A parallel digital processor system for particle image velocimetry. *Meas. Sci. Technol.*, 4:619–626, 1993.

[17] M. Mercier, M. Grondeau, S. Guillou, J. Thiébot, and E. Poizot. Towards the modelling of turbulence at tidal stream power sites with the lattice boltzmann method. *EWTEC*, 2017.

27

[18] P. Mycek, B. Gaurier, G. Germain, G. Pinon, and E. Rivolaen. Experimental study of the turbulence intensity effects on marine current turbines behaviour. part I: One single turbine. *Renew. Energ.*, 66:729–746, 2014.

[19] P. Saha, G. Biswas, A.C. Mandal, and S. Sarkar. Investigation of coherent structure in a turbulent channel with built-in longitudinal vortex generator. *Int. J. Heat Mass Trans.*, 104:178–198, 2017.

[20] K. Sarkar and B.S. Mazmunder. Turbulent flow over the trough region formed by a pair of forward-facing bedform shapes. *European J. of Mechanics B/Fluids*, 46:126–143, 2014.

[21] SHOM. MNT bathymétrique de façade atlantique (projet homonim). 2015.

[22] L. Sirovich. Turbulence and the dynamics of coherent structures. part I: Coherent structures. *Q Appl. Math.*, XLV:561–571, 1987.

[23] B.W. Van Oudheusen, F. Scarano, N.P. Van Hinsberg, and D.W. Watt. Phase-resolved characterization of vortex shedding in the near wake of a square-section cylinder at incidence. *Exp. Fluids*, 39:86–98, 2005.

[24] J. Wallace. Quadrant analysis in turbulence research: history and evolution. *Annu. Rev. Fluid Mech.*, 48:131–158, 2016.

[25] J. Wallace, H. Eckelmann, and R. Brodkey. The wall region in turbulent shear flow. *J. Fluid Mech.*, 54:39–48, 1972.

[26] J. Westerweel and F. Scarano. Universal outlier detection for PIV data. *Exp. Fluids*, 39:1096–1100, 2005.

[27] J.N. Wood, G. De Nayer, S. Schmidt, and M. Breuer. Experimental investigation and large-eddy simulation of the turbulent flow past a smooth and rigid hemisphere. *Flow Turbul. Combust.*, 1:79–119, 2016.

Highlights for paper entitled: *Experimental analysis of the floor inclination effect on the turbulent wake developing behind a wall mounted cube:*

- Tests are carried out on a wall-mounted cube with and without an inclined floor representative of seabed elements, in Froude similitude with high Reynolds number,

- PIV measurements are perfomed in horizontal and vertical measurement planes and spatial analyses are performed,

- POD filter and quadrant analyses show the rise of coherent energetic structures.